Citation: Xiaotian Xia, Ju Han. Analysis of multi-tooth contact characteristics of cycloidal pinwheel mechanism based on photoelasticity principle. *Journal of Harbin Institute of Technology (New Series)*. DOI: 10.11916/j.issn.1005-9113.2024027.

Analysis of Multi-Tooth Contact Characteristics of Cycloidal Pinwheel Mechanism Based on Photoelasticity Principle

*Xiaotian Xia and Ju Han**

(*College of Mechanical Engineering, North China University of Science and Technology, Tangshan 063000, Hebei, China*)

Abstract: The contact characteristics between cycloidal gear teeth and pinwheel teeth significantly impact the operational performance of cycloidal pinwheel mechanisms. Current research methods tend to rely primarily on theoretical calculations, with limited use of experimental methods for detecting dynamic contact properties. We propose a novel method for testing the dynamic contact characteristics of cycloidal pinwheel mechanisms. By combining Hertzian contact theory and contact strength theory, we establish a force and meshing stiffness model for the cycloidal and pinwheel gears, and determine the maximum contact stress and variations in pinwheel gear force and meshing stiffness. Based on the principle of photoelasticity, we built a testing platform for the cycloidal pinwheel mechanism to assess its contact characteristics. This platform provides the stress distribution of the cycloidal pinwheel mechanism and allows us to deduce key parameters such as the number of meshing teeth and the meshing interval. This study provides an experimental method for investigating the contact characteristics of cycloidal pinwheel mechanisms.

Keywords: cycloidal pinwheel mechanisms; Hertzian contact theory; contact characteristics; principles of photoelasticity

CLC number: TH132.41 **Document code**: A **Article ID**: 1005-9113(2024)00-0000-10

0 Introduction

The cycloidal pinwheel mechanism, a crucial component of the RV reducer, significantly contributes to achieving a large transmission ratio. Renowned for its high transmission accuracy, substantial bearing capacity, and exceptional impact resistance, the RV reducer has become a vital component in industrial joint robots and precision machine tool transmissions[1]. The force profile of the cycloidal gear tooth has a substantial impact on the transmission error of the RV reducer, and is intimately linked to contact deformation[2]. Currently, there are no experimental testing methods for analyzing the contact characteristics of cycloidal pinwheel mechanisms. This paper introduces an experimental method to detect the contact characteristics between cycloidal wheels and pinwheel teeth.

To further enhance the performance of the cycloidal pinwheel mechanism, domestic and international researchers have conducted extensive research on the meshing characteristics of this mechanism, yielding significant findings. Zhang et al.[3] developed a nonlinear mechanical model of the meshing pair using the super-static method, and deduced the variation of the meshing force over time based on the equal power relationship between the meshing force and resistance moment. They further transformed the meshing force into an elliptical distributed load acting on the contact area. Brovkina et al.[4] employed techniques for automatically calculating the gap and deformation between cycloid meshing teeth and teeth, and analyzed the effects of tooth profile correction on the gap and deformation, as well as the number of teeth simultaneously transmitting load. Yu et al.[5] utilized the finite element method to investigate the specific influence of manufacturing errors-induced gaps on the meshing force, thereby providing guidance for manufacturing

Received 2024-03-01.

Sponsored by the Natural Science Foundation of Hebei Province (Grant No. E2019209153), the Tangshan Science and Technology Program (Grant No. 22130219G).

* Corresponding author: Ju Han, Associate Professor, Ph.d in Mechanical Engineering. Email: hanju@ncst.edu.cn.

accuracy requirements. Li et al.[6] took into account the initial meshing clearance between the pinwheel tooth and cycloidal gear, and the contact deformation generated during meshing. They deduced the distribution law of the contact load on the cycloidal gear under transient conditions. Through the utilization of Finite Element (FE) and dynamic multi-body analysis, Tariq et al[7] evaluated and compared the kinematics equivalents between the traditional cycloidal pinwheel drive and its involute teeth, while also examined the stress of the cycloidal pinwheel mechanism. Xu et al.[8] advanced a comprehensive dynamic analysis approach grounded in multi-body dynamics theory and elastic contact theory, which could accurately predict the meshing quantity in cycloidal pinwheel mechanism, and identify the contact point, and determine the contact load. By incorporating Hertz contact theory, bending moment equilibrium equation, and deformation compatibility condition, Zhou et al.[9] developed a loaded tooth contact analysis model for composite cycloid. Hsieh et al.[10] investigated the meshing contact and collision dynamic traits of cycloidal transmission tooth profile and analyzed the strength of crucial components in the transmission. Jiang et al.[11] have introduced a novel approach that integrates conformal mapping of multiple interconnected regions with the proposed global scale factor in order to enhance the precision of intricate geometric shapes, such as cycloidal gears, and to conduct an analysis on the stress distribution within cycloidal gears. Li et al.[12] established a geometric model of cycloidal pinwheel mechanism utilizing three-dimensional design software and analyzed the contact load and stress distribution during the meshing process of cycloidal pinwheel teeth through the application of finite element technology. Taking into account the influence of crank bearing, pinwheel hole clearance, and cycloidal tooth profile modification, Chang et al.[13] analyzed the contact characteristics of associated contact pairs in cycloidal pinwheel mechanism. Wu et al.[14] proposed a novel approach for optimizing the tooth profile modification of cycloidal pinion reducer. The mechanical analysis model utilized the optimized modification to consider pinion force, bearing force, transmission ratio, and transmission error. Based on no-load Tooth Contact Analysis (TCA) and nonlinear Hertz contact theory, Li et al.[15-16] proposed a method to calculate the meshing stiffness of cycloidal pinwheel pairs. Ren et al.[17] computed the meshing stiffness of cycloidal gear and pinwheel gear, considering the force deformation of cycloidal gear teeth and Hertz contact theory. The aforementioned studies have established a crucial theoretical foundation for examining the multi-tooth contact characteristics of cycloidal pinwheel mechanisms. Current research on the contact characteristics between cycloidal wheels and pinwheel teeth primarily relies on theoretical analysis, with few methods available to measure the meshing characteristics directly.

This paper introduced an experimental method for detecting contact characteristics using the photoelastic principle. A force analysis model for the cycloidal wheel and pinwheel is established, using MATLAB to calculate the maximum force and stiffness variations for each tooth profile and pinwheel tooth. Polycarbonate was chosen as the experimental medium due to its optical and mechanical properties. The photoelastic principle was employed to deduce the relationship between stress and dark spot distribution. Experiments reveal the stress at various positions on the cycloidal wheel, the number of gear engagements, and the meshing range of the cycloidal pinwheel mechanism.

1 Testing Equipment and Principle

1.1 Photoelasticity Principle

The photoelastic method is an effective technique for describing the stress and strain of complex geometric structures under varying loads. It is currently the most widely used stress-strain measurement method. When transparent isotropic media are subjected to external forces, their refractive index changes result in optical anisotropy. Uneven stress distribution within the medium causes inconsistent birefringence, leading to varying phase differences in light waves passing through different locations. Light sources with these differing phase differences display different colors.

In the context of a polarized light field, the photoelasticity model under load exhibits birefringence, necessitating the use of an isotropic material. Consequently, polycarbonate is selected as the material for the cycloidal needle wheel mechanism model. As illustrated in Fig. 1, natural light passing through the polarizer and 1/4 wave plate generates plane polarized light. When this plane polarized light is vertically incident upon a loaded plane model, the

two principal stresses, σ_1 and σ_2, at a specific point on the model are resolved into two plane polarized lights with distinct velocities. These two distinct plane polarized lights generate a relative optical path difference Δ. The relationship between the sum of the principal stresses and the optical path difference Δ is outlined as in Eq.(1).

$$\sigma_1 - \sigma_2 = \frac{\Delta}{\delta(c_1 - c_2)} = \frac{f}{\delta}N \tag{1}$$

where $N = \Delta/\lambda$ is the isometric fringe series, $f = \lambda/c_1 - c_2$ is the fringe value of photoelasticity material, δ is the model thickness, λ is the light source wavelength, $(c_1 - c_2)$ is the stress optical constant.

$$f = \frac{8P}{\pi \cdot D \cdot N} \tag{2}$$

where D is the disc diameter, P is the external load.

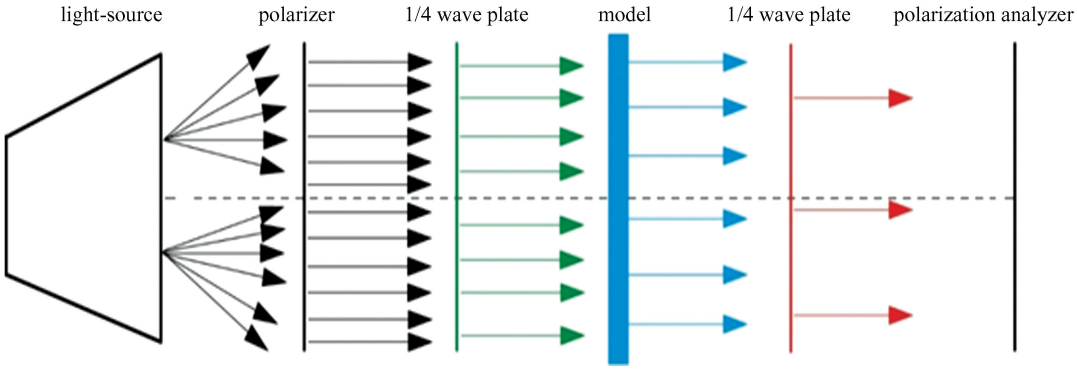

Fig.1 Photoelasticity schematic diagram

1.2 Experimental Platform

To detect the changes in contact characteristics between a cycloidal wheel and a pinwheel during movement, this study proposed an experimental method based on the photoelastic principle. As shown in Fig.2, an experimental platform is established to analyze these contact characteristics. The cycloidal pinwheel mechanism is rotated by an electric motor. The optical phenomenon resulting from the birefringence effect of the cycloidal gears and pinwheel teeth is observed through two polarizers. This phenomenon is captured by a camera situated on the right side of the experimental platform. The photoelasticity experiment should be conducted in a low-light environment, using white light and monochromatic light as sources. The camera captures the birefringent effect of the cycloidal gear model driven by the motor.

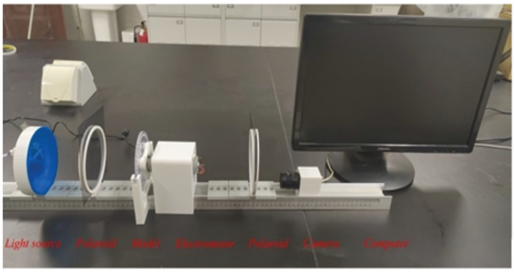

Fig.2 Experimental platform

2 Mathematical Model of Cycloid Pinwheel Mechanism

2.1 Cycloid Pinwheel Contour Equation

The cycloidal needle wheel mechanism is composed of a needle wheel, a cycloidal wheel, and a crank. Due to manufacturing and processing errors, as well as assembly errors, there may be interference in the motion process of the cycloidal pinwheel mechanism under no-load conditions[18]. Theoretically, there should be no gap between the standard cycloidal gear teeth and the pinwheel teeth. However, to ensure the normal operation of the cycloidal pinwheel mechanism, the cycloidal gear tooth profile must be modified[19-20].

The dynamic coordinate system $O_P X_P Y_P$, the fixed coordinate system $O_P XY$, and the static coordinate system $O_c X_c Y_c$ are established as illustrated in Fig. 3, adhering to the right-hand rule. The cycloidal gear tooth profile is generated by the needle wheel rolling on the pitch circle. The tooth profile equation of the needle wheel is as follows:

$$R'_{\mathrm{p}} = \begin{bmatrix} r_{\mathrm{rp}}\cos\theta \\ r_{\mathrm{rp}}\sin\theta + r_{\mathrm{p}} \\ 1 \end{bmatrix} \tag{3}$$

where r_{p} is the pinwheel distribution circle radius

(mm), θ is the needle wheel rolling angle (°), r_{rp} is the wheel radius (mm).

The cycloidal gear tooth profile equation is derived through a coordinate system transformation, with the coordinate change matrix outlined as in Eq.(4).

$$\boldsymbol{M}_{pc}=\begin{bmatrix}\cos\varphi & \sin\varphi & -e\sin\left(\dfrac{Z_p\varphi}{Z_p-Z_c}\right)\\ -\sin\varphi & \cos\varphi & -e\cos\left(\dfrac{Z_p\varphi}{Z_p-Z_c}\right)\\ 0 & 0 & 1\end{bmatrix} \tag{4}$$

where e is the eccentricity (mm), the parameter e represents the distance between the center of the cycloidal wheel and the center of the pin wheel. φ is the angle corresponding to the contact point of cycloidal gear teeth (°), Z_p and Z_c is the number of pinwheel teeth and cycloidal gear teeth. The number of cycloidal gearteeth does not equate to the number of pinwheel teeth ($Z_p > Z_c$), with a difference of 1 being the most commonly employed value ($Z_p - Z_c = 1$).

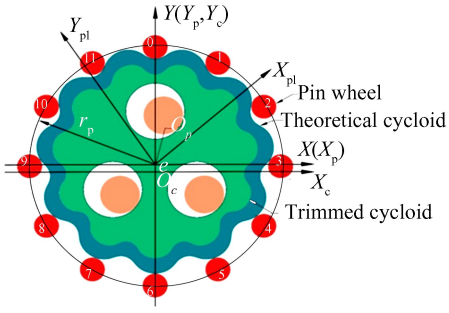

Fig.3 Cycloid needle wheel mechanism diagram

By employing matrix operations, the profile curve of the modified cycloidal gear can be derived as in Eq.(5).

$$\boldsymbol{R}_c=\begin{bmatrix}(r_p+\Delta r_p)\sin\varphi-e\sin(Z_p\varphi)+(r_{rp}+\Delta r_{rp})(\lambda\sin(Z_p\varphi)-\sin\varphi)S\\ (r_p+\Delta r_p)\cos\varphi-e\cos(Z_p\varphi)-(r_{rp}+\Delta r_{rp})(-\lambda\cos(Z_p\varphi)+\cos\varphi)S\\ 1\end{bmatrix} \tag{5}$$

where Δr_p is the moved distance modification (mm), Δr_{rp} is the equidistance modification (mm), $\lambda = eZ_1/(r_p+\Delta r_p)$ is the curtate ratio, $S=(1+k^2-2k\cos(Z_c\varphi))^{-\frac{1}{2}}$.

Modification methods for cycloidal wheels can be obtained based on the varying sizes of parameters, such as Δr_p and Δr_{rp}. To date, the most extensively employed approach is the negative equidistant-shift modification.

According to the recent findings of the cycloidal pinwheel mechanism research, the prevalent parameters associated with the cycloidal pinwheel mechanism are enumerated as in Table 1.

Table 1 Common parameters of cycloidal pinwheel mechanism

Radius of the distribution circle of the balance wheel r_p (mm)	Needle Wheel Radius r_{rp} (mm)	Needle wheel radius Δr_p (mm)	Shift trimming amount Δr_{rp} (mm)	Equidistant trimming quantity Z_p	Number of cycloid teeth Z_c	Eccentricity e (mm)	Rated input load (N·mm)	Rated speed of cycloidal wheel (r/min)
52	2	0.015	0.005	39	40	0.9	167	15

2.2 Hertz Contact Theory

Hertz contact theory is a prevalent approach to establish the contact model of cycloidal pinwheel teeth. Based on this foundation, the influence of reducer parameters on meshing stiffness can be further delved into. As illustrated in Fig.4, during the process of contact between the cycloidal wheel and the needle wheel, the cycloidal wheel contour can be considered as a cylinder. According to the Hertz contact theory, the deformation area and the total deformation formula of the contact area of the double cylinder can be derived.

$$b=\sqrt{\frac{4F\rho}{\pi B E^*}} \tag{6}$$

$$\delta=\frac{F}{\pi B}\left[\frac{1-\nu_1^2}{E_1}\left(\ln\frac{4\rho_1}{b}-\frac{1}{2}\right)+\frac{1-\nu_2^2}{E_2}\left(\ln\frac{4\rho_2}{b}-\frac{1}{2}\right)\right] \tag{7}$$

where E_1, E_2 and v_1, v_2 are the elastic modulus and Poisson ratio, E^* and ρ are the equivalent elastic modulus and equivalent radius of curvature (mm), B is the cycloid wheel height (mm), F is the external load (N), ρ_1 and ρ_2 is the radius of curvature of cycloidal gear teeth and pinwheel teeth (1/mm).

$$\begin{cases}\dfrac{1}{E^*}=\dfrac{(1-\nu_1^2)}{E_1}+\dfrac{(1-\nu_2^2)}{E_2}\\ \rho=\dfrac{R_1R_2}{R_1\pm R_2}\end{cases} \tag{8}$$

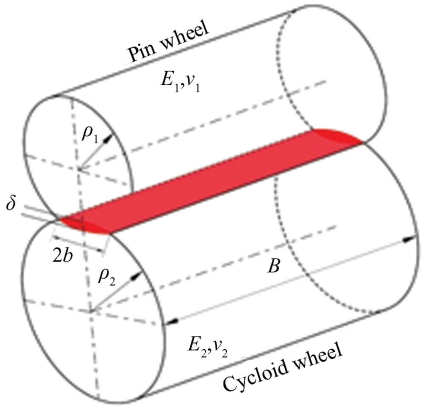

Fig.4 Hertz contact model

In the process of contact between cycloidal gear teeth and pinwheel teeth, because the changes of contact area size and elastic deformation are very small, and the change of curvature is quite limited, it can be assumed that the radius of curvature remains unchanged during the contact process. According to Hertz's theorem, we can solve the distribution curve of the deformation δ_i of cycloidal gear teeth and needle teeth.

$$\delta_i = \frac{\sin \varphi_i}{\sqrt{1 + k^2 - 2k\cos \varphi_i}} \delta_{\text{nmax}} \tag{9}$$

where φ_i is the Y_1 axis rotation angle of the cycloidal wheel relative to the coordinate system $O_1 X_1 Y_1$, δ_{nmax} is the maximum deflection.

2.3 Load-Bearing Contact Analysis of Cycloidal Needle Wheel

The torque that propels the motion of the cycloidal pinwheel mechanism is transferred to the cycloidal gear via the crank bearing. A portion of the torque facilitates the rotation of the cycloidal gear, while the remainder of the torque is transformed into deformation force during the engagement between the cycloidal gear tooth profile and the needle tooth. Based on the deformation of the tooth profile and the input torque, the equilibrium equation of force and torque can be derived as Eq.(10).

$$\begin{cases} T = \sum F_{ci} l_i \\ F_{ci} = K_i \delta_i \end{cases} \tag{10}$$

where F_{ci} is the contact force on cycloid wheel (N), T is the input torque applied to a cycloidal pinwheel mechanism (N · mm), l_i is the contact force arm (mm).

Let (x_c, y_c) denote the coordinates of the initial contact point, (x_z, y_z) represent the coordinates of the initial contact point corresponding to the center of the pinwheel, and β_c denote the corresponding correction angle.

The cycloidal pinwheel's initial contact force arm profile exhibits in Eq.(11).

$$l_i = \frac{\left| \begin{matrix} (y_c - y_z)(e + \triangle e)\sin(\beta_c) + (x_z - x_c) \\ (e + \triangle e)\cos(\beta_c) + y_z x_c - y_c x_z \end{matrix} \right|}{\sqrt{(y_c - y_z)^2 + (x_z - x_c)^2}} \tag{11}$$

The initial contact profile of the cycloidal wheel experiences deformation due to applied force. This deformation serves to mitigate the inter-tooth profile gap. Upon elimination of the profile gap, the corresponding tooth profile undergoes contact deformation. It is crucial to note that the other contact profiles should be arrayed on either side of the initial contact profile with the number of contacts being contingent on the input torque.

The coordinates of the second contact point (x_{c1}, y_{c1}), corresponding to the center of the needle wheel, are denoted as (x_{z1}, y_{z1}). Let β_c represent the corresponding correction angle, and δ_0 denote the deformation of the first contact point. The position of the second contact point and the position of the first contact point are identical, as is the position of the point P. The coordinates of the P point are as Eq.(12).

$$\begin{cases} x_p = \dfrac{y_c x_p - y_p x_c}{x_p - x_c + (y_c - y_p)\tan \beta_c} \tan \beta_c \\ y_p = \dfrac{y_c x_p - y_p x_c}{x_p - x_c - (y_c - y_p)\tan \beta_c} \end{cases} \tag{12}$$

The force arm of the secondary contact tooth profile within the cycloidal pinwheel mechanism is Eq.(13).

$$l_i = \frac{\left| \begin{matrix} (y_p - y_{z1})(e + \triangle e)\sin(\beta_c) + (x_{z1} - x_p) \\ (e + \triangle e)\cos(\beta_c) + y_{z1} x_p - y_p x_{z1} \end{matrix} \right|}{\sqrt{(y_p - y_{z1})^2 + (x_{z1} - x_p)^2}} \tag{13}$$

The nonlinearity of the cycloidal wheel's stiffness is attributed to its material properties and geometric configuration. Consequently, altering parameters, such as the modification amount of the cycloidal wheel, will influence its stiffness. According to the definition of stiffness, the formula for the cycloidal wheel's stiffness K can be derived as follows:

$$K_i = \frac{F}{\delta} = \frac{\pi l}{\left[\dfrac{1 - \nu_1^2}{E_1} \left(\ln \dfrac{4R_1}{b} - \dfrac{1}{2} \right) + \dfrac{1 - \nu_2^2}{E_2} \left(\ln \dfrac{4R_2}{b} - \dfrac{1}{2} \right) \right]} \tag{14}$$

The materials employed in the photoelasticity

experiment for cycloidal gears and needle teeth differ from those used in practical applications, resulting in distinct stiffness and deformation characteristics. In order to facilitate a more comprehensive investigation of the motion behavior of cycloidal needle wheel mechanisms, the deformation properties of both practical and experimental materials are standardized.

$$\delta_{gs} = \frac{F_s}{K_s} = \frac{F_g}{K_g} \tag{15}$$

where δ_{gs} is the deformation of cycloidal gear and needle tooth, F_s and F_g are the force of cycloidal gear and needle tooth under actual and photoelasticity experimental conditions, K_s and K_g are the stiffness of cycloidal gear and pinwheel tooth under actual and photoelasticity experimental conditions.

2.4 Analysis of Force Range of Cycloid Pinwheel

The interface between the cycloidal wheel and the needle wheel is characterized by line contact, resulting in a three-way compression stress state. Employing the third and fourth strength theories, we can determine the equivalent stress state values individually. Based on the stress distribution characteristics of line contact, the stress intensity at the contact center point can be derived utilizing the fourth strength theory:

$$\begin{cases} \sigma_{c1} = -0.5\, q_{max} \\ \sigma_{c2} = \sigma_{c3} = -q_{max} \end{cases} \tag{16}$$

The equivalent stress is σ_{eq} can be calculated using the following formula.

$$\sigma_{eq} = \sqrt{\frac{1}{2}[(\sigma_{c1}-\sigma_{c2})^2 + (\sigma_{c2}-\sigma_{c3})^2 + (\sigma_{c3}-\sigma_{c1})^2]} = 0.5\, q_{max} \tag{17}$$

The third strength theory is employed to address the equivalent stress, with the focus on the stress at the contact center point, as shown τ_{max} is as follows:

$$\begin{cases} \sigma_{c1} = -0.26\, q_{max} \\ \sigma_{c2} = -0.2 q_{max} \\ \sigma_{c3} = -0.8 q_{max} \end{cases} \tag{18}$$

The maximum shear stress τ_{max} is in Eq.(19).

$$\tau_{max} = \frac{\sigma_{c1} - \sigma_{c3}}{2} = 0.27\, q_{max} \tag{19}$$

The equivalent stress is as shown in Eq.(20).

$$\sigma_{eq} = \sigma_{c1} - \sigma_{c3} = 0.54\, q_{max} \tag{20}$$

Yield strength check is as shown in Eqs.(21) and (22).

$$\sigma_{eq} < \sigma_s = q_{max} \tag{21}$$

$$\sigma_{eq} = m q_{max} < [\sigma_c] \tag{22}$$

where m is the equivalence factor. The maximum force that each tooth profile of the cycloid pinwheel mechanism can withstand has been determined. The maximum contact effort solution formula of cycloidal gear tooth profile is as follows:

$$F_{max} = \frac{\pi b\, l_i\, [\sigma_c]}{2m} \tag{23}$$

When the cycloidal wheel comes into contact with the needle wheel, the primary load is radial load, and the dominant deformation mode is contact deformation. Given the negligible impact of other deformations, such as shear deformation, this study exclusively focuses on contact deformation. The meshing force F_j, representing the interaction between the jth tooth profile of the modified cycloidal gear and the associated cycloidal wheel, can be expressed as follows:

$$F_j = \frac{\delta_j - \triangle \varphi_i}{\delta_{max}} F_{max} \tag{24}$$

where δ_{max} is the maximum deflection, δ_j is the jth tooth profile deformation. The contact stress σ_i associated with the meshing state of the jth tooth profile of the modified cycloidal gear can be articulately expressed in Eq.(25).

$$\sigma_i = \sqrt{\frac{F_j\left(\frac{1}{\rho_j} \pm \frac{1}{r_{rp}}\right)}{2\pi b\left(\frac{1-v^2}{E}\right)}} \tag{25}$$

where ρ_j is the radius of curvature at the jth meshing point.

According to the design parameters and material properties of the cycloidal wheel and the needle wheel, the maximum force and maximum torque of the cycloidal needle wheel under maximum working conditions are calculated, allowing for the determination of the working load of the cycloidal needle wheel mechanism.

3 Data Analysis

3.1 Theoretical Data Analysis

Based on the aforementioned analytical model, MATLAB and MASTA were utilized to analyze the maximum force and stiffness variation of the pinwheel teeth during the motion of the cycloidal pinwheel mechanism. As illustrated in Fig.5(a), the distribution of the maximum force experienced by the pinwheel tooth during the rotation of the cycloidal gear centers around the pinwheel tooth distribution circle. In each cycle, the force applied to the pinwheel tooth

initially increases and then decreases, with the rate of increase being noticeably slower than that of the decrease. This suggests that the contact process between the pinwheel tooth and the cycloidal gear is more gradual than the detachment process. As shown in Fig.5(b), the change in pinwheel tooth stiffness closely follows the change in pinwheel tooth force, indicating that the variation in the curvature of the cycloidal gear tooth profile and the pinwheel tooth has minimal impact on the force experienced by both.

In Fig.6, different colors represent different needle wheels. The force change diagram for each pinwheel tooth at a specific moment is presented in Fig.6(a). The force distribution on the pinwheel teeth shows a decreasing trend from the center of the maximum force pinwheel tooth to its adjacent regions on both sides. The force on the pinwheel teeth that rotate in the same direction as the cycloid gear remains relatively stable, with minimal variation between adjacent pinwheel teeth and a small force difference between the two sides of each pinwheel tooth. In contrast, the force fluctuation is significant for the maximum force pinwheel tooth and for pinwheel teeth rotating in the opposite direction to the cycloid gear. The force change between adjacent pinwheel teeth is relatively large with a significant force difference between the two sides of each pinwheel tooth.

As illustrated in Fig.6(b), the stiffness distribution of each pinwheel tooth at a specific time is shown. The stiffness distribution exhibits a decreasing trend from the center of the maximum force pinwheel tooth to both sides. A notable change in the stiffness of the 37th pinwheel tooth is observed, along with some pinwheel tooth profiles that are not under stress, which suggests that the 37th pinwheel tooth is gradually separating from the contact tooth profile. The stiffness changes in other stressed pinwheel teeth are relatively stable, with only small differences in stiffness among them.

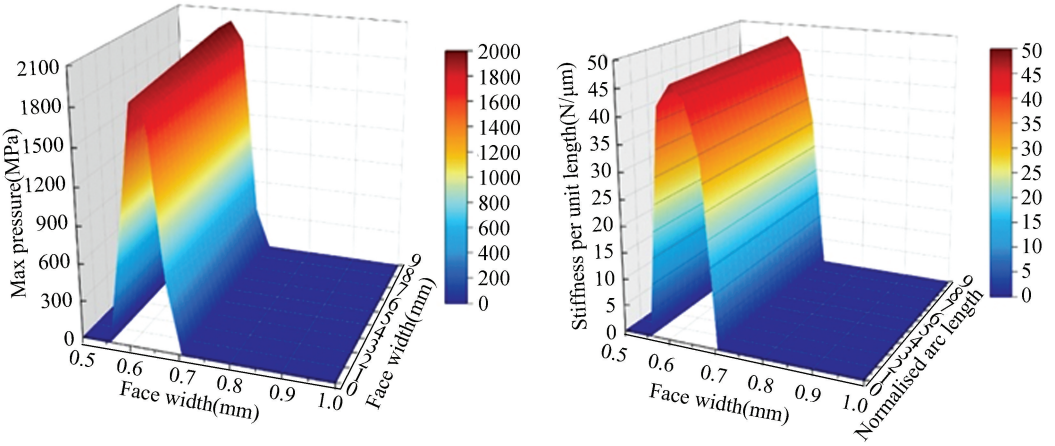

(a) Max pressure (b) Stiffness per unit length

Fig.5 Single needle tooth force diagram

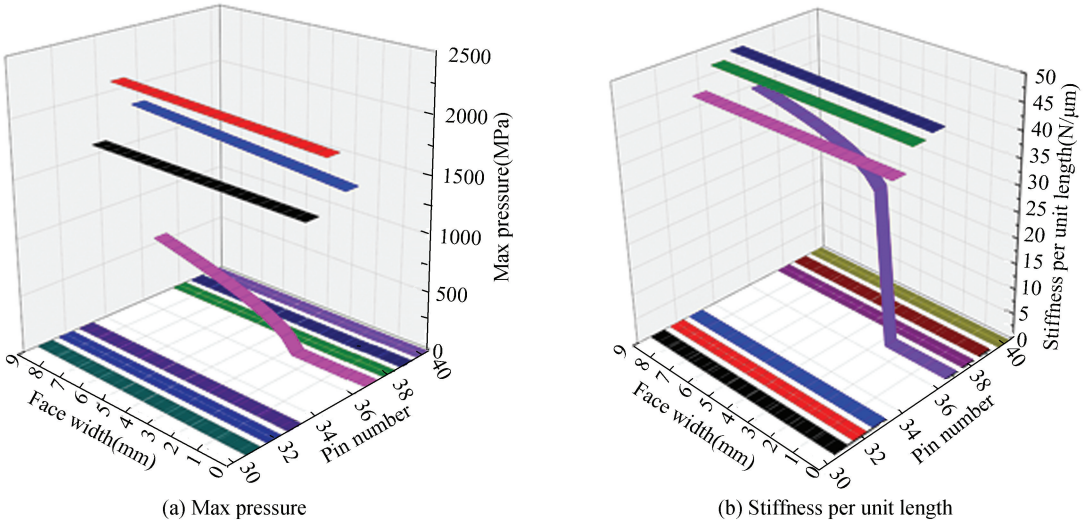

(a) Max pressure (b) Stiffness per unit length

Fig.6 The force and stiffness change diagram of the whole needle tooth

The contact force between the cycloid gear and the pinwheel tooth at a specific moment under the rated load is depicted in Fig.7. It is evident that the force on the middle two tooth profiles is significantly greater than that on the two side tooth profiles. As shown in Fig. 7, the force on the tooth profiles gradually increases and then gradually decreases during the rotation process. Consequently, the force process of the cycloidal gear tooth profile can be characterized as a flexible meshing process.

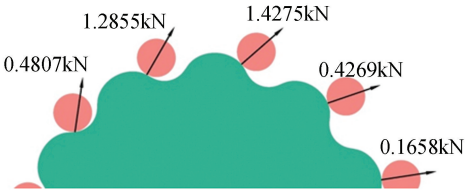

Fig.7 Local tooth profile force

3.2 Test Date Analysis

By investigating the optical phenomena of cycloidal wheels and needle wheels under various stress conditions, we can determine the force profile, force position, and force size data, which provides a theoretical basis for further analyzing the cycloidal needle wheel mechanism. As depicted in Fig.8, the optical properties of polycarbonate materials exhibit variations in response to external forces. With increasing stress, the optical phenomena transition from a singular profile to a dual profile.

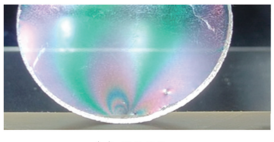

(a) 20 N•m

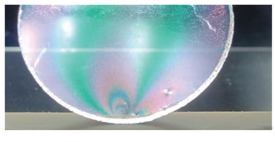

(b) 30 N•m

Fig.8 30 cm circular force diagram

The optical phenomena resulting from the birefringence effect of the cycloidal wheel at different positions are illustrated in Fig.9. It is evident that varying positions lead to distinct optical effects. Considering the inherent processing stress of the material, the initial color of the cycloidal wheel appears as pink. Upon application of force, its color changes successively to light green, light purple, green, purple, yellow, and blue. As the position of the cycloidal needle roller mechanism changes, so does the distribution of force on its tooth profiles. Fig.9 depicts the force distribution at various positions of both the cycloidal wheel and the needle roller. During their contact, the maximum force is exerted on the second tooth profile in the early and middle stages. In the later stages, the maximum force shifts to the third tooth profile. The birefringence effect of white light produces a range of colors, as shown in Fig.9. White light consists of multiple wavelengths (λ), each corresponding to a distinct force. By conducting experiments using various colored light sources, it is possible to accurately determine the forces at each position. Fig.10 depicts a fringe pattern model under a blue light source for the cycloid needle roller mechanism.

As shown in Fig.9, there are five teeth involved in the initial engagement process between the cycloidal wheel and the pinwheel, and six teeth involved in other engagement stages. Additionally, the contour tooth tip and tooth root of the cycloidal wheel do not participate in the meshing process of the cycloidal pinwheel mechanism. By synthesizing Figs. 8 and 9, it is determined that the engagement interval of the cycloidal pinwheel mechanism is [5.5, 7.3].

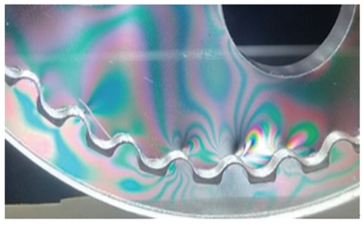

(a) Front

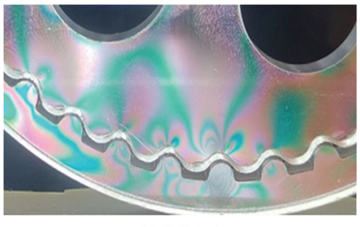

(b) Middle

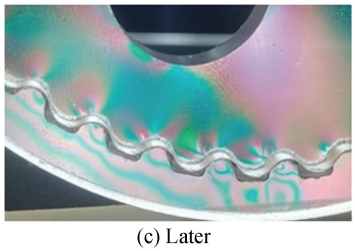

(c) Later

Fig.9 Cycloidal wheel photoelasticity experiment

Fig.10 illustrates the force distribution within the cycloidal pinwheel during the contact process of the cycloidal pinwheel mechanism. The optical fringes generated by the cycloidal gear model under blue light illumination are depicted in Fig.10, with the meshing point as the focal point, demonstrating a circular distribution of fringes. According to Eq.(1) and Eq.(2), the force at any position of the cycloidal pinwheel mechanism can be calculated. Based on the principles of photoelasticity and contour fringe series, the force range for the tooth profile in Fig.10, from left to right, is as follows: 28.4-42.6 N, 71-85.2 N, 71-85.2 N, and 42.6-56.8 N. Upon determining the force range under various light sources, the ultimate force is established by replacing the light sources of different colors.

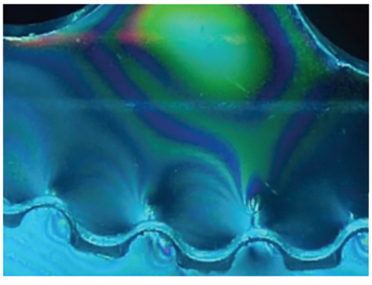

Fig.10 Blue light source cycloidal needle wheel model fringe pattern

4 Conclusions

A method is introduced to evaluate the contact characteristics between cycloidal gears and pinwheel teeth using photoelastic theory. A stress analysis model that considers the contact deformation of the cycloidal wheel and pinwheel is established. The load amplitude corresponding to the experimental material is calculated under a constant input load. Experiments determine the number of meshing teeth and the meshing interval of the cycloidal pinwheel mechanism. The following conclusions are drawn from this research.

1) The coloration of the cycloidal wheel and needle wheel, fabricated from polycarbonate material, alters to light green, light purple, green, purple, etc., upon application of force, with distinct force levels corresponding to each hue.

2) As the external load on the cycloidal pinwheel mechanism increases, the force on the tooth profile of the mechanism also intensifies. With increasing stress, the optical phenomena transition from a singular profile to a dual profile. In the tooth profile of cycloidal pinwheel mechanism, the force on the middle tooth profile is larger, and the force on both sides of the tooth profile is smaller. The force exerted on the epicyclic gear is evenly distributed in a circular pattern, with the point of meshing serving as the central focal point.

3) During the meshing process, the stiffness of the pinwheel teeth varies, with distinct stiffness levels at various positions. The root and tip of the cycloidal gear tooth profile do not participate in the contact process. The inner engagement interval between the cycloidal wheel and the pinwheel is [5.5, 7.3], with 5 to 6 teeth involved in the meshing process of the cycloidal pinwheel mechanism.

References

[1] Taldenko Y K. Mathematical model of planetary roller-tooth reduction gears. Chemical and Petroleum Engineering, 1994, 30: 145 - 153. DOI: 10.1007/BF01149777.

[2] Malhotra S K, Parameswaran M A. Analysis of a cycloid speed reducer. Mechanism and Machine Theory, 1983, 18(6):491-499. DOI: 10.1016/0094-114X(83)90066-6.

[3] Zhang P, An Z. Research on nonlinear mechanical properties for engagement pair of cycloid ball planetary transmission. Engineering Mechanics, 2010, 27(3):186-192.

[4] Brovkina Y I, Sobolev A N, Nekrasov A Y. Research of characteristics and parameters of cycloidal gear. Proceedings of the 4th International Conference on Industrial Engineering. Berlin: Springer, 2018: 1169 - 1179. DOI: 10.1007/978-3-319-95630-5_122.

[5] Yu H, Liu G, Wang Y, et al. The impact of gap on meshing force in two-stage cycloidal gear drive. 2017 IEEE International Conference on Information and Automation. Piscataway: IEEE, 2017: 760 - 763. DOI: 10.1109/ICInfA.2017.8079006.

[6] Li L, He W, Wang X, et al. Research on high precision RV transmission for robots. Journal of Dalian Railway Institute, 1999, 20: 1-11.

[7] Tariq H, Galym Z, Amrin A, et al. Assessment of contact forces and stresses, torque ripple and efficiency of a cycloidal gear drive and its involute kinematical equivalent. Mechanics Based Design of Structures and Machines, 2024, 52: 1304 - 1323. DOI: 10.1080/15397734.2022.2144885.

[8] Xu L, Yang Y. A general method for multi-tooth contact analysis of cycloid-pin gear transmission. China Mechanical Engineering, 2016, 27: 1382. DOI: 10.3969/

j.issn.1004-132X.2016.10.017.

[9] Zhou S, Han Z, Zhou Y, et al. Load tooth contact analysis of composite cycloidal planetary transmission with small tooth difference. 2023 IEEE 12th Data Driven Control and Learning Systems Conference. Piscataway: IEEE, 2023: 1991-1996. DOI: 10.1109/DDCLS58216.2023.10166206.

[10] Hsieh C F. Dynamics analysis of cycloidal speed reducers with pinwheel and nonpinwheel designs. Journal of Mechanical Design, 2014, 136(9): 091008. DOI: 10.1115/1.4027850.

[11] Jiang N, Jiang L, Zhang J, et al. A novel method for the analysis and optimization of end face stress in cycloidal gears based on conformal mapping. Applied Sciences, 2023, 13(21): 11805. DOI:10.3390/app132111805.

[12] Li S. Design and strength analysis methods of the trochoidal gear reducers. Mechanism and Machine Theory, 2014, 81: 140-154. DOI: 10.1016/j.mechmachtheory.2014.07.001.

[13] Chang L, Tsai S, Huang C. Contact characteristics of cycloid planetary gear drives considering backlashes and clearances. Forschung im Ingenieurwesen, 2022, 86: 337-356. DOI:10.1007/s10010-021-00535-1.

[14] Wu S, Guo R, Li X. Quasi-static force analysis and tooth profile modification optimization of the cycloid speed reducer. Applied Sciences, 2024, 14(2): 845. DOI: 10.3390/app14020845. DOI:3390/app14020845.

[15] Li X, Chen B, Wang Y, et al. Mesh stiffness calculation of cycloid-pin gear pair with tooth profile modification and eccentricity error. Journal of Central South University, 2018, 25: 1717-1731. DOI: 10.1007/s11771-018-3863-z.

[16] Li X, Li C, Wang Y, et al. Analysis of a cycloid speed reducer considering tooth profile modification and clearance-fit output mechanism. Journal of Mechanical Design, 2017, 139(3): 033303. DOI: 10.1115/1.4035541.

[17] Ren Z, Mao S, Guo W, et al. Tooth modification and dynamic performance of the cycloidal drive. Mechanical Systems and Signal Processing, 2017, 85: 857-866. DOI: 10.1016/j.ymssp.2016.09.029.

[18] Li T, Tian M, Xu H, et al. Meshing contact analysis of cycloidal-pin gear in RV reducer considering the influence of manufacturing error. Journal of the Brazilian Society of Mechanical Sciences and Engineering, 2020, 42: 133. DOI:10.1007/s40430-020-2208-7.

[19] Han J, Li W, Qiao Z. Lubrication characteristics of cycloid pin wheel transmission of RV reducer. Journal of Central South University, 2021, 28: 398-417. DOI:10.1007/s11771-021-4611-3.

[20] Su J, Zhang H, Jiang C, et al. Prediction and experimental study on thermal stress in multi-tooth form grinding of cycloid gear. The International Journal of Advanced Manufacturing Technology, 2021, 117: 187-198. DOI:10.1007/s00170-021-07677-0.